

# Photoacoustically guided wavefront shaping for enhanced optical focusing in scattering media

Puxiang Lai<sup>†</sup>, Lidai Wang<sup>†</sup>, Jian Wei Tay<sup>†</sup> and Lihong V. Wang<sup>\*</sup>

**Non-invasively focusing light into strongly scattering media, such as biological tissue, is highly desirable but challenging. Recently, ultrasonically guided wavefront-shaping technologies have been developed to address this limitation. So far, the focusing resolution of most implementations has been limited by acoustic diffraction. Here, we introduce nonlinear photoacoustically guided wavefront shaping (PAWS), which achieves optical diffraction-limited focusing in scattering media. We develop an efficient dual-pulse excitation approach to generate strong nonlinear photoacoustic signals based on the Grueneisen relaxation effect. These nonlinear photoacoustic signals are used as feedback to guide iterative wavefront optimization. As a result, light is effectively focused to a single optical speckle grain on the scale of 5–7  $\mu\text{m}$ , which is  $\sim 10$  times smaller than the acoustic focus, with an enhancement factor of  $\sim 6,000$  in peak fluence. This technology has the potential to benefit many applications that require a highly confined strong optical focus in tissue.**

The scattering of light by wavelength-scale refractive index changes is the reason why media such as paper, frosted glass, fog and biological tissue appear opaque<sup>1</sup>. The distortion of the optical wavefront propagating within such scattering media makes conventional lens focusing impossible at depths, as the optical wavelets no longer add up in phase at the targeted position. This phenomenon fundamentally limits high-resolution optical imaging techniques such as two-photon microscopy and optical coherence tomography to depths up to a single transport mean free path ( $\sim 1$  mm in soft tissue)<sup>2</sup>. Invasive procedures, such as embedding optical fibres, are often resorted to when concentrated light is desired beyond this depth, such as in optogenetics<sup>3</sup> and photothermal therapy<sup>4</sup>. When coherent light propagates in a scattering medium, speckles are formed. Despite the random appearance of speckles, the way that light is scattered is deterministic within the speckle correlation time. This property has spurred recent advances in optical time-reversal and wavefront-shaping<sup>5</sup> techniques to manipulate the optical wavefront and form a focus within a scattering medium.

Optical time-reversal focusing is achieved by sensing and phase-conjugating the re-emitted wavefront either from an internal virtual guide star provided by focused ultrasound (TRUE<sup>6–13</sup> and TROVE<sup>14</sup>) or second harmonic radiation emitted by nanoparticles<sup>15</sup>, or from a physical guide star provided by embedded fluorescent particles<sup>16</sup>. In contrast, wavefront-shaping focusing is achieved by optimizing the incident wavefront to maximize the signal from a guide star. This pattern can be found using iterative algorithms<sup>17–19</sup> or by measuring the so-called ‘transmission matrix’<sup>20</sup>. For absorptive targets, photoacoustic sensing is preferred<sup>21–25</sup>, because the signal comes directly from the target and it is non-harmful and non-invasive.

To date, focusing by photoacoustically guided wavefront shaping (PAWS) has usually produced acoustic diffraction-limited spots. Here, we show that it is possible to beat the acoustic diffraction limit and focus light to a single optical speckle grain. We use a novel mechanism to obtain a nonlinear photoacoustic signal based on an effect we call the Grueneisen relaxation effect (to be defined later). Unlike most other nonlinear phenomena, this new

mechanism produces nonlinear signals in a highly efficient manner, enabling detection with a high signal-to-noise ratio (SNR). Using this nonlinear signal as feedback, PAWS achieves single speckle-grain focusing, even when a large number of speckle grains are present within the acoustic focus. We demonstrate this principle and show a clear optical focus on the scale of 5–7  $\mu\text{m}$ , which is  $\sim 10$  times smaller than the acoustic focus, with an enhancement of peak fluence ( $\text{J m}^{-2}$ ) by a factor of  $\sim 6,000$ .

## Principle

The photoacoustic effect describes the formation of acoustic waves due to the absorption of light, which is usually short pulsed. The photoacoustic amplitude is proportional to the absorbed optical energy density, where the coefficient is given by the local Grueneisen parameter. It is well known that the Grueneisen parameters of many materials are highly temperature-dependent. For example, from 25 °C to 40 °C the Grueneisen parameters of water and blood can increase by 58 and 76%, respectively<sup>2,26</sup>. Within the thermal confinement time, the temperature rise due to the absorption of light lingers and changes the local Grueneisen parameter accordingly, a phenomenon referred to as the ‘Grueneisen relaxation effect’.

Here, we use a dual-pulse excitation approach to obtain a nonlinear photoacoustic signal based on the Grueneisen relaxation effect. As shown in Fig. 1a, two identical laser pulses are fired sequentially to excite the same absorber. At the first laser pulse, the Grueneisen parameter is determined by the initial temperature. At the second laser pulse, the Grueneisen parameter is changed (usually increased) due to the Grueneisen relaxation effect. Accordingly, the second photoacoustic signal differs from the first in amplitude. If we assume that the photoacoustic amplitude is proportional to the laser energy and the Grueneisen parameter is linearly dependent on the local temperature, the amplitude difference between the two photoacoustic signals is proportional to the square of the laser energy (or fluence), yielding a nonlinear signal despite the fact that both original photoacoustic signals are generated linearly with the current optical fluence. A detailed derivation is provided in the following.

Optical Imaging Laboratory, Department of Biomedical Engineering, Washington University in St Louis, St. Louis, Missouri 63130-4899, USA. <sup>†</sup>These authors contributed equally to this work. \*e-mail: lhwang@wustl.edu

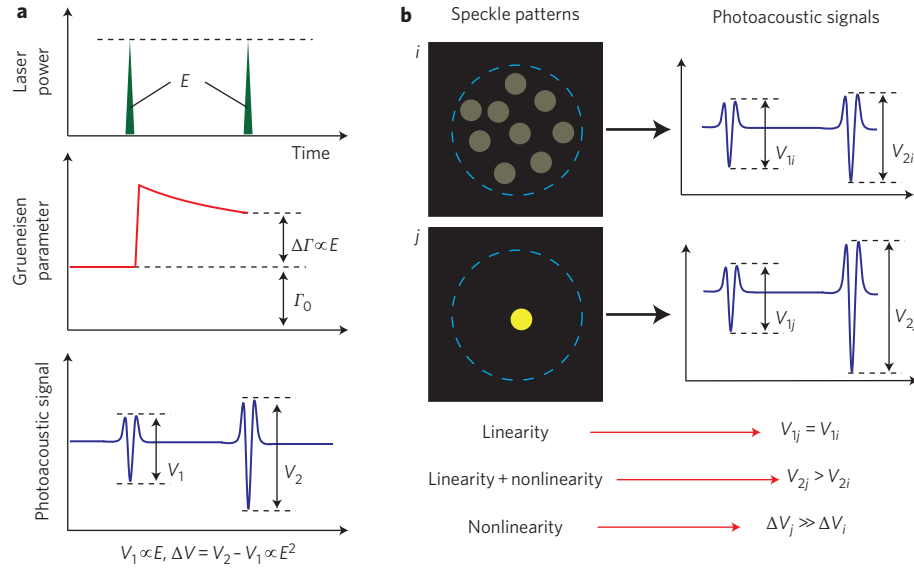


**Figure 1 | Principles.** **a**, Illustration of dual-pulse excitation producing a nonlinear photoacoustic signal based on the Grueneisen relaxation effect. Two laser pulses with equal energy  $E$  are incident on an optical absorber. The first pulse causes a lingering change in the Grueneisen parameter ( $\Delta\Gamma$ ) due to an increase in temperature. Within the thermal confinement time,  $\Delta\Gamma$  causes the amplitude from the second photoacoustic signal ( $V_2$ ) to be stronger than that from the first ( $V_1$ ). The difference  $\Delta V$  is nonlinear, being proportional to the square of the laser pulse energy (or fluence). **b**, Illustration of the nonlinear PAWS principle. When the same optical energy is concentrated to fewer speckle grains within an acoustic focus, the linear photoacoustic amplitude does not increase significantly, but the nonlinear photoacoustic amplitude approximately increases in inverse proportion with the number of bright speckle grains. Blue dashed circles represent the ultrasonic focal region.

The peak-to-peak amplitude of the first photoacoustic signal is given by the integral

$$V_1 = k \iint A(x, y) \Gamma_0 \mu_a F(x, y) dx dy \quad (1)$$

where  $k$  is a constant coefficient,  $A(x, y)$  is the acoustic detection sensitivity distribution normalized as  $\iint A(x, y) dx dy = 1$ ,  $\Gamma_0$  is the Grueneisen parameter at the initial temperature ( $T_0$ ),  $\mu_a$  is the material absorption coefficient, and  $F(x, y)$  is the optical fluence distribution. From here on, all photoacoustic amplitudes refer to peak-to-peak values. Within the acoustic resolution voxel, both  $\Gamma_0$  and  $\mu_a$  are assumed to be uniform and constant, and the integration along the  $z$ -axis direction is taken into account in coefficient  $k$ .  $A(x, y)$  is frequently approximated using a Gaussian function,  $A(x, y) = (1/2\pi w^2) \exp[-(x^2 + y^2)/2w^2]$ , where  $2\sqrt{\ln 2} w$  is the full-width at half-maximum (FWHM) of the one-way transducer response.

The Grueneisen parameter immediately before the second laser pulse can be approximated as

$$\Gamma = \Gamma_0 + \eta \Gamma'_0 \mu_a F \quad (2)$$

where  $\eta$  is a constant coefficient that converts absorbed optical energy density into temperature rise and  $\Gamma'_0$  is the first-order derivative of the Grueneisen parameter with respect to temperature at  $T_0$ . Therefore, the amplitude of the second photoacoustic signal is

$$V_2 = k \iint A(x, y) [\Gamma_0 + \eta \Gamma'_0 \mu_a F(x, y)] \mu_a F(x, y) dx dy \quad (3)$$

The amplitude difference between the two photoacoustic signals is

$$\Delta V = V_2 - V_1 = k \eta \Gamma'_0 \mu_a^2 \iint A(x, y) F^2(x, y) dx dy \quad (4)$$

This amplitude difference  $\Delta V$  is determined by the square of the optical fluence, so we refer to it as the ‘nonlinear photoacoustic amplitude’.

When the amplitude from a single photoacoustic signal is used as feedback to iterative wavefront shaping (which we term ‘linear

PAWS’), optical energy is concentrated into the acoustic focus<sup>21,22,24,25</sup>. To focus light to a single speckle grain, we use the nonlinear photoacoustic amplitude  $\Delta V$  as feedback (which we term ‘nonlinear PAWS’). The reason for the narrower optical focus can be explained by rewriting equation (4) as

$$\Delta V = k \eta \Gamma'_0 \mu_a^2 (\bar{F}^2 + \sigma_F^2) \quad (5)$$

where  $\bar{F} = \iint A(x, y) F(x, y) dx dy$  and  $\sigma_F^2 = \iint A(x, y) [F(x, y) - \bar{F}]^2 dx dy$  can be treated as the mean and variance of  $F(x, y)$ , with a probability density function of  $A(x, y)$ . As both  $\bar{F}^2$  and  $\sigma_F^2$  are non-negative,  $\Delta V$  is maximized when both  $\bar{F}^2$  and  $\sigma_F^2$  are maximized.  $\bar{F}^2$  is proportional to  $V_1^2$  and therefore reaches its maximum when light is concentrated within the acoustic focus. Consequentially, if the total optical energy is constrained,  $\sigma_F^2$  is maximized when all the optical energy is focused to a single speckle grain.

Figure 1b further explains why nonlinear PAWS can focus light to a single speckle grain using an idealized example. We simplify the ultrasonic detection sensitivity to a relatively uniform distribution within a circular focal area and assume that the total light energy is constant and evenly distributed among the speckle grains within the acoustic focus. Let us consider two different speckle patterns  $i$  and  $j$ : speckle pattern  $i$  has multiple speckle grains within the ultrasonic focus and speckle pattern  $j$  has only one speckle grain. In these two cases, the two linear photoacoustic amplitudes  $V_{1i}$  and  $V_{1j}$  are the same, but the two nonlinear photoacoustic amplitudes  $\Delta V_i$  and  $\Delta V_j$  are significantly different. Compared with speckle pattern  $i$ , speckle pattern  $j$  concentrates light onto a smaller area and thus causes a higher temperature rise, resulting in a strong nonlinear photoacoustic signal. If all speckle grains have the same area, from equation (4) the nonlinear photoacoustic amplitude can be simply expressed as

$$\Delta V = \frac{1}{M} k \eta \Gamma'_0 \mu_a^2 A_0 \frac{E^2}{s^2} \quad (6)$$

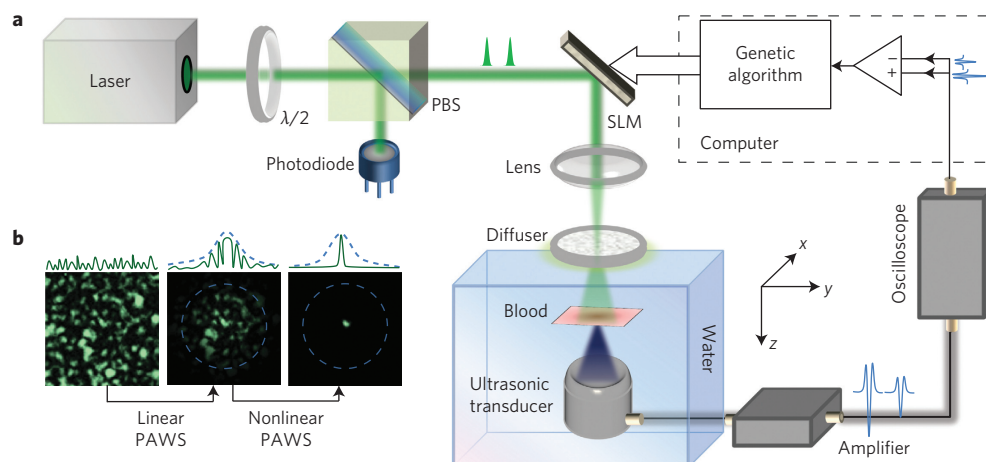


**Figure 2 | Experimental set-up and dual-stage optimization.** **a**, Schematic of the PAWS experimental set-up. PBS, polarized beamsplitter; SLM, spatial light modulator;  $\lambda/2$ , half-wave plate. **b**, Illustration of the two-stage optimization procedure (see Supplementary Movies 1 and 2 for more information). Stage 1: linear PAWS focuses light into the acoustic focal region. Stage 2: nonlinear PAWS focuses light onto a single-speckle grain. Blue dashed circles represent the acoustic focal region. A typical intensity distribution (green solid line) is shown above the speckle illustrations. Blue dashed envelopes represent acoustic sensitivity.

where  $M$  is the number of speckle grains (or optical modes) within the acoustic focus,  $A_0$  is the constant acoustic detection sensitivity,  $E$  is the total pulse energy, and  $s$  is the area of one speckle grain. Equation (6) shows that the nonlinear photoacoustic amplitude  $\Delta V$  is inversely proportional to  $M$  and is maximized when  $M = 1$  (optical speckle-scale focusing). The peak fluence [ $\sim E/(Ms)$ ] is also inversely proportional to  $M$ . The nonlinear photoacoustic amplitude is therefore proportional to the peak fluence at constant incident laser energy. Although this conclusion is based on idealized assumptions, it is helpful for estimating the order of magnitude of the peak fluence.

### Experimental results

The PAWS set-up is illustrated schematically in Fig. 2a. The scattering medium consisted of a ground glass diffuser and a layer of optically absorbing whole blood. The incident light reflected from the spatial light modulator (SLM) surface was scattered by the diffuser, generating a random speckle pattern with  $\sim 5 \mu\text{m}$  speckle grains on the blood layer. A photodiode monitored the energy of each laser pulse to compensate for the variations in the photoacoustic signals. The pulse energy on the blood layer was  $\sim 0.1 \text{ mJ}$ , within an illuminated area of  $\sim 1 \text{ cm}^2$ , corresponding to a fluence of  $\sim 0.1 \text{ mJ cm}^{-2}$ . Initially, no nonlinear photoacoustic signals were observable, even at the full energy output of the laser. To generate detectable nonlinear photoacoustic signals, the optical fluence needs to be sufficiently high. Therefore, to increase the optical fluence within the photoacoustic sensing region, we first conducted linear PAWS (stage 1) before nonlinear PAWS (stage 2), as illustrated in Fig. 2b and Supplementary Movies 1 and 2. For both stages, the SLM was divided into  $192 \times 108$  independently controlled blocks. The optimization of the phase pattern on the SLM was implemented with a genetic algorithm<sup>19,27,28</sup>.

In linear PAWS (stage 1), single laser pulses were fired every 20 ms to generate the photoacoustic signals. An initial photoacoustic signal (inset of Fig. 3a), averaged over 16 traces, was recorded by displaying a random phase pattern on the SLM. As shown in Fig. 3b, the photoacoustic amplitude increased as the linear PAWS optimization proceeded, corresponding to increased optical energy within the acoustic focus<sup>21,25</sup>. The algorithm was terminated after 800 iterations when the improvement was less than 5% over 100 iterations and, by the end, the photoacoustic amplitude had increased  $\sim 60$  times over the initial signal (Fig. 3a). We estimated that the

fluence within the acoustic focus had increased from  $\sim 0.1$  to  $\sim 6 \text{ mJ cm}^{-2}$ . The last  $\sim 250$  iterations with linear PAWS showed diminishing returns, as indicated by the relatively flat response towards the end.

The final phase map from stage 1 was used as the starting point for nonlinear PAWS (stage 2). In the nonlinear PAWS experiment we fired a pair of pulses (separated by  $40 \mu\text{s}$ , limited by the maximum laser repetition rate) within the thermal confinement time  $\tau_{\text{th}}$  of  $\sim 192 \mu\text{s}$  (estimated from  $\tau_{\text{th}} = d^2/\alpha_{\text{th}}$ , where the dimension of the heated region,  $d$ , was estimated as a speckle size of  $\sim 5 \mu\text{m}$  and the thermal diffusivity  $\alpha_{\text{th}}$  was  $\sim 1.3 \times 10^{-3} \text{ cm}^2 \text{ s}^{-1}$ ). The initial photoacoustic signal pair, obtained using the phase map from stage 1, is presented in Fig. 4a. The final photoacoustic signal pair after 1,600 iterations is shown in Fig. 4b, which also shows the optimized phase pattern displayed on the SLM (see inset). The enhancement of the nonlinear photoacoustic amplitude with iteration in stage 2 is shown in Fig. 4c. The last 250 iterations improved the enhancement factor by only 5%. As seen, the final nonlinear photoacoustic amplitude was  $\sim 100$  times greater than the initial value, indicating an  $\sim 100$  times improvement in the peak fluence. To avoid overheating of the blood during optimization, the laser energy was attenuated by 10% every 300 iterations. At the beginning of each adjustment,  $\Delta V$  was remeasured. All other parameters were kept constant. The change in energy was compensated for in the results shown in Fig. 4b,c. The nonlinear signal plateaued towards the end of the optimization, indicating that the focal spot had approached its smallest size.

We imaged the optical field at the ultrasonic focal plane using a charge-coupled device (CCD) camera. When a random phase pattern was displayed on the SLM, a speckle pattern (Fig. 5a) was captured with randomly distributed speckle grains. The FWHM of the acoustic focus is shown by the dashed circle. Note that there are many speckle grains within the acoustic focus. When the optimized phase pattern from nonlinear PAWS was displayed, a focal spot with the size of a single speckle grain was formed (Fig. 5b). The size of the focal spot was measured to be  $5.1 \mu\text{m} \times 7.1 \mu\text{m}$  (FWHM), which is  $\sim 10$  times smaller than that of the acoustic focus.

### Discussion

To date, most optical focusing studies using PAWS have been limited by acoustic diffraction when extended optical absorbers are targeted. To break through the acoustic resolution limit, we

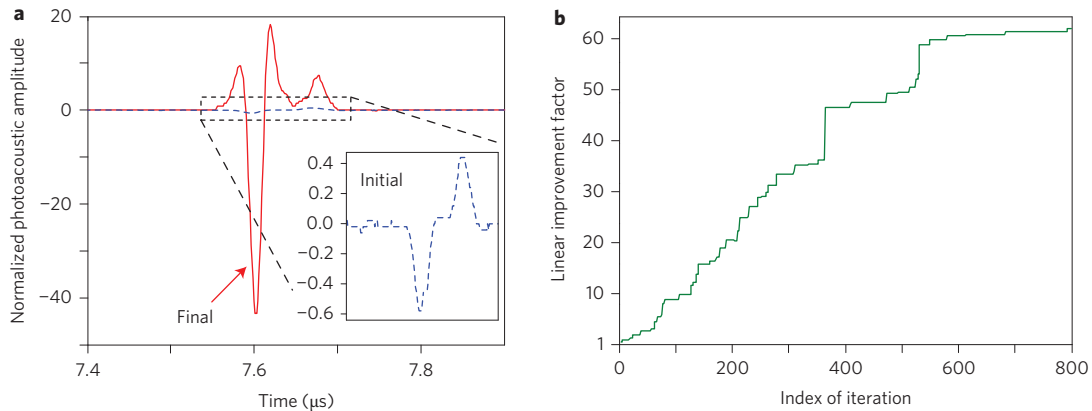


**Figure 3 | Experimental results of stage 1: using a linear photoacoustic signal as feedback for wavefront shaping (linear PAWS).** **a**, Photoacoustic signals before (blue dashed curve) and after (red solid curve) the linear PAWS (stage 1) optimization. Note that all photoacoustic signals in this study were compensated for laser energy fluctuations, and normalized to the initial photoacoustic peak-to-peak amplitude shown here. **b**, Linear improvement factor (defined as the ratio of the photoacoustic amplitudes and the initial photoacoustic amplitude) versus iteration index. Linear photoacoustic amplitude improved  $\sim 60$  times in stage 1, indicating a peak enhancement factor of  $\sim 60$  for optical fluence within the acoustic focus.

have proposed and demonstrated nonlinear PAWS. Using dual-pulse excitation, nonlinear photoacoustic signals were generated based on the Grueneisen relaxation effect. Although most nonlinear phenomena are weak, photoacoustic nonlinearity based on the Grueneisen relaxation effect is exceptionally strong due to the dependence (primarily) of the thermal expansion coefficient and (secondarily) of the speed of sound on temperature<sup>26,29,30</sup>. As shown in Fig. 4b, the nonlinear signal  $\Delta V$  was even stronger than the first linear signal  $V_1$ . It is worth noting that both of the original photoacoustic signals are produced linearly with the current incident laser fluence, and subtraction recovers the nonlinear signal component. This strong nonlinear photoacoustic phenomenon observed using dual-pulse excitation and based on the Grueneisen relaxation effect is likely to find broad applications in biomedical optics.

By maximizing the nonlinear photoacoustic amplitude we were able to focus diffuse light into a single optical speckle grain. The focus was measured to be  $5.1 \mu\text{m} \times 7.1 \mu\text{m}$ , about an order of magnitude smaller than the acoustic focal size in the linear dimension. Note that about 169 speckle grains existed within the acoustic focal region (estimated by taking the ratio between the area of the acoustic focus and the area of a single speckle grain), but after nonlinear PAWS, only one became dominant.

The peak fluence enhancement in our study was estimated to be a factor of  $\sim 6,000$ ,  $\sim 60$  times from the linear PAWS stage (Fig. 3) and  $\sim 100$  times from the nonlinear PAWS stage (Fig. 4). Moreover, the peak fluence enhancement can also be estimated from the temperature rise. At the end of the nonlinear PAWS, the second photoacoustic amplitude  $V_2$  was  $\sim 168\%$  greater than the first photoacoustic amplitude  $V_1$ , which was measured at room temperature ( $25^\circ\text{C}$ , Fig. 4b). Assuming that the Grueneisen parameter of blood is proportional to the temperature rise<sup>26</sup>, we estimate the corresponding instantaneous temperature rise to be  $\sim 33^\circ\text{C}$ . Note that instantaneous (submillisecond) temperature rises of this magnitude do not cause biological damage<sup>31</sup>. From this, we predict the final fluence  $F$  to be

$$F = \frac{\Delta T \rho C_V}{\mu_a} = \frac{33 \text{ K} \times 1 \text{ g cm}^{-3} \times 3,600 \text{ J g}^{-1} \text{ K}^{-1}}{240 \text{ cm}^{-1}} = 495 \text{ mJ cm}^{-2} \quad (7)$$

where  $\rho$  is the mass density of blood,  $C_V$  is the heat capacitance of blood, and  $\mu_a$  is the absorption coefficient of blood. Compared to

the initial fluence of  $\sim 0.1 \text{ mJ cm}^{-2}$ , the final peak fluence is increased by a factor of  $\sim 4,950$ , which agrees reasonably with the aforementioned estimate of  $\sim 6,000$ .

The expected peak improvement factor for phase-only (that is, no amplitude optimization) wavefront shaping is given by<sup>5,12</sup>

$$\text{Factor} = \frac{\pi N - 1}{4 M} + 1 \quad (8)$$

where  $N$  is the number of independently controlled SLM blocks ( $192 \times 108$  in our study) and  $M$  is the number of optical speckle grains (optical modes) within the acoustic focus ( $\sim 169$  in the linear PAWS stage). Thus, the theoretical enhancement ratio from the linear PAWS was 97. Experimentally, we measured an enhancement of  $\sim 60$  (Fig. 2b). The difference could be due to laser-mode fluctuation, non-uniformity of optical illumination on the SLM, stray light, mechanical instability of the system and measurement errors. Nonetheless, after linear PAWS, the optical fluence within the acoustic focus was sufficient to generate detectable nonlinear photoacoustic signals. After nonlinear PAWS, the number of bright speckle grains should ideally be reduced from  $\sim 169$  to 1. Hence, we expected an improvement factor of  $\sim 169$  after nonlinear PAWS. In the experiment, the improvement was  $\sim 100$  (Fig. 4c). The less than expected performance was probably due to the same factors affecting linear PAWS. The peak fluence enhancement of  $\sim 6,000$  is also approximately consistent with the expected improvement factor from equation (8), when  $M$  after nonlinear PAWS was reduced to  $\sim 2$  to 3, counting the ‘residual’ darker speckle grains in Fig. 5b.

To date, there have been only two other demonstrations of non-invasive speckle-scale optical focusing inside scattering media. One makes use of time reversal of variance-encoded light in a technique called TROVE<sup>14</sup>. In TROVE, the scattered light is recorded with multiple illumination speckle realizations while a focused ultrasound beam is used to define the target region. Speckle-scale focusing is then obtained by computing the appropriate phase map from the measured speckle fields. Achieving similar goals, TROVE and nonlinear PAWS are complementary. TROVE time-reverses ultrasonically encoded light, and is therefore more applicable for non- or low-absorption targets. In comparison, nonlinear PAWS is preferred in applications with optically absorptive targets, such as blood vessels or melanomas in biological tissue. Furthermore, the peak enhancement reported in TROVE is  $\sim 110$ , whereas we have demonstrated an unprecedented peak enhancement of  $\sim 6,000$ .

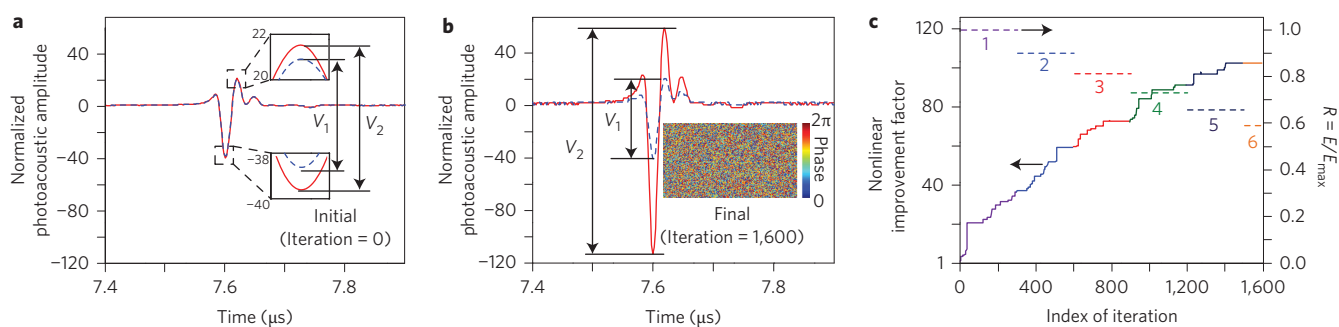


**Figure 4 | Experimental results of stage 2: using a nonlinear photoacoustic signal as feedback for wavefront shaping (nonlinear PAWS).** **a**, The initial photoacoustic signal pair (blue dashed curve for the first and red solid curve for the second) from the paired laser pulses. The difference between the two photoacoustic signal amplitudes,  $\Delta V$ , was used as feedback in nonlinear PAWS. **b**, The final photoacoustic signal pair (blue dashed curve for the first; red solid curve for the second) after stage 2 optimization. Inset: final optimized phase pattern displayed on the SLM. **c**, Nonlinear improvement factor versus iteration index. The normalized laser energy  $R = E/E_{\max}$  is also shown, where  $E$  is the incident laser energy and  $E_{\max}$  is the initial laser energy used before adjustment. The compensated nonlinear photoacoustic amplitudes are given by  $\Delta V/R^2$ , and the nonlinear improvement factor is therefore given by  $(\Delta V/R^2)/\Delta V_{\text{initial}}$ , where  $\Delta V_{\text{initial}}$  is the initial  $\Delta V$ .

Sub-acoustic-resolution optical focusing using linear PAWS was recently demonstrated by Conkey and co-authors<sup>23</sup>. They used the spatial sensitivity profile of an ultrasonic transducer to discriminate signal contributions between different speckle grains within the detection region. However, their system requires a relatively high detection SNR. Otherwise, the number of speckle grains within the ultrasonic focus is restricted, for example, to less than 10, as was shown. It remains to be seen whether this approach is superior to direct detection using a higher-frequency ultrasonic transducer.

As with many other implementations in the field<sup>5,14,19,21,22,25,28,32</sup>, our method has not yet been applied to thick living biological tissue. The main technological hurdles are the slow optimization speed and the ratio of the number of independently controlled elements on the SLM to the number of speckle grains within the detection area in tissue.

Linear and nonlinear PAWS currently take a total of several hours to complete. To maintain the deterministic property of the scattering medium, the PAWS focusing procedure must be completed within the speckle decorrelation time, which is on the order of 1 ms for *in vivo* tissue due to physiological motion such as blood flow and respiration. We are currently limited by the number of iterations required for the optimization. The algorithm took 800 iterations for linear PAWS and 1,600 iterations for nonlinear PAWS. Each iteration required 15 measurements<sup>19,28</sup>, each of which took about 1.2 s to acquire. The long acquisition time was due in part to the 0.5 s it took for the SLM display to be updated (this is partly due to software-timed updating of the image and driver characteristics, which was beyond our control) and the 0.7 s needed to acquire, average (over 16 times to assure sufficient detection SNR), transfer and process each measurement. It therefore took  $\sim(0.5 + 0.7) \times 15 \times 800 = 4$  h and  $(0.5 + 0.7) \times 15 \times 1,600 = 8$  h for linear and nonlinear PAWS, respectively. Due to this long optimization time, we demonstrated the principle using a stable diffuser. In the future, faster devices can be used to accelerate the optimization. For example, digital mirror devices with switching times of 22  $\mu$ s have been used in wavefront shaping<sup>33</sup> and could shorten the optimization. The speed also affects our choice of the number of controlled blocks used on the SLM. On the one hand, the optimization time with the genetic algorithm scales linearly with the number of blocks<sup>19,28</sup>. On the other hand, the potential peak enhancement also increases linearly. We chose to use  $192 \times 108$  as a practical compromise.

Another challenge occurs when the scattering medium is sufficiently thick that, inside it, the speckle grain size approaches the order of half the optical wavelength, much smaller than the

5  $\mu$ m in the present study. This diminution results in a much greater number of speckle grains within the acoustic focal region, which, according to equation (8), reduces the performance (that is, the peak intensity enhancement) expected from linear PAWS, which may further hinder the generation of nonlinear photoacoustic signals with sufficient SNR. Nevertheless, if more pixels on the SLM can be controlled independently (especially after the optimization speed is significantly improved), or a strong nonlinear photoacoustic signal can be generated directly without prefocusing from linear PAWS, optical focusing in thick biological tissues would be possible. Therefore, the orders-of-magnitude peak enhancement with a well-defined virtual guide star achieved in nonlinear PAWS has the potential to advance many laser applications in tissues, such as laser microsurgery and single-neuron optogenetic activation, that benefit from intense and highly confined focusing.

It should also be pointed out that the generation of a nonlinear photoacoustic signal requires only a moderate instantaneous (rather than continuous) temperature rise. We used an initial fluence of 6  $\text{mJ cm}^{-2}$  for nonlinear PAWS, which is well below the ANSI safety limit of 20  $\text{mJ cm}^{-2}$  (ref. 34). To avoid potential thermal damage, the laser energy was attenuated during the nonlinear optimization. On the one hand, because nonlinear PAWS successfully proceeded with fluences as low as 6  $\text{mJ cm}^{-2}$ , the laser energy could be further reduced. On the other hand, the high optical fluence after nonlinear PAWS could potentially be leveraged for laser microsurgery at optical resolution in tissue.

In this Article, we assume that the nonlinear photoacoustic signal is quadratic with the laser pulse energy, based on the linear temperature dependence of the Grueneisen parameter. However, even in the presence of higher-order effects, nonlinear PAWS can still lead to optical speckle-scale focusing. It should also be noted that the optical focal spot produced using nonlinear PAWS is near the centre of the acoustic focus. However, the precision is limited by the SNR of the final photoacoustic signals and the exact acoustic focal profile.

We have demonstrated a nonlinear PAWS approach to break the acoustic resolution limit and achieve both optical resolution focusing and a high peak enhancement factor in scattering media. While the present study was performed using whole blood as the absorbing target, the Grueneisen relaxation effect exists broadly in many materials<sup>35</sup>. Therefore, similar performance can be anticipated with other types of absorber. Furthermore, the system can conceivably be engineered to respond much faster. Doing so would allow nonlinear PAWS to open an avenue for many micrometre-scale

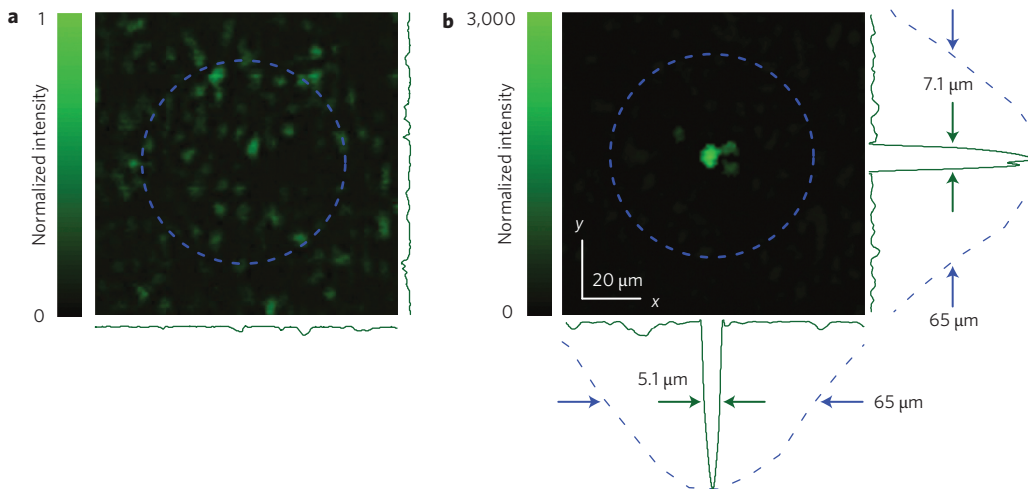


**Figure 5 | Visualization of single speckle grain focusing using nonlinear PAWS.** **a**, Speckle pattern observed behind the diffuser when a randomized phase pattern is displayed on the SLM. **b**, Optical focus down to a single speckle grain observed behind the diffuser when the optimized phase pattern from stage 2 (Fig. 4b, inset) is displayed on the SLM. The one-dimensional profiles across the focus (green solid curves) measure 5.1 and 7.1  $\mu\text{m}$  along  $x$  and  $y$ , respectively. Blue dashed circles show the measured acoustic focal region (50 MHz,  $-6$  dB). Its lateral profiles (blue dashed curves) measure a FWHM of 65  $\mu\text{m}$ . The intensity values in **a** and **b** are normalized to the peak value in **a**, after correction for the different camera settings for the two images.

optical applications, including imaging, sensing, therapy and manipulation, inside highly scattering biological tissue.

## Methods

**Experimental set-up.** The experimental set-up is illustrated schematically in Fig. 2a, with more details shown in Supplementary Fig. 1. We used a 532 nm pulsed laser (INNOSLAB BX2II-E, EdgeWave GmbH), which produced 10 ns pulses (pulse energy  $\leq 0.2$  mJ) at an adjustable pulse repetition rate of 0–30 kHz. The laser beam was directed through a half-wave plate and a polarizing beamsplitter to sample a small fraction of the beam. Light reflected by the beamsplitter was attenuated and measured using a photodiode (PDA36A, Thorlabs) and was used to compensate for energy fluctuations of the laser output. Light transmitted by the beamsplitter was expanded and then reflected off a liquid-crystal-on-silicon (LCoS)-based phase-only SLM (PLUTO, Holoeye Photonics). The SLM had an aperture of 16 mm  $\times$  9 mm, with a resolution of 1,920  $\times$  1,080 pixels. In the experiment, the SLM was evenly divided into 192  $\times$  108 blocks, each independently controlled, with a linearized<sup>36</sup> phase shift between 0 and  $2\pi$ . The reflected beam was condensed using a set of lenses, and focused by a microscopic objective ( $\times 10$ , NA = 0.25) onto a ground glass diffuser (DG10-120, Thorlabs; the turbidity of the diffuser is illustrated in Supplementary Fig. 2). A neutral density filter wheel between the SLM and the objective lens reduced the laser fluence in nonlinear PAWS experiments to avoid thermal saturation. A circular container (15 mm diameter, 4 mm height) of bovine blood was placed 10 mm away from the diffuser to serve as the absorptive target for photoacoustic sensing. A focused ultrasonic transducer (home made, based on a non-focusing transducer) was positioned on the other side of the blood layer to detect the photoacoustic signal. Both the blood layer and ultrasonic transducer were immersed in water for acoustic coupling. The water was maintained at room temperature by circulation.

**Detection of photoacoustic signals and control of optimization.** The photoacoustic signals generated were amplified by 50 dB (ZFL-500LN+ and ZX60-43-S+, Mini-Circuits), digitized and averaged by an oscilloscope (TDS5034, Tektronix) at a bandwidth larger than 500 MHz and sent to a computer. The linear and nonlinear photoacoustic amplitudes were quantified in MATLAB (R2012b, MathWorks) and a genetic algorithm<sup>19,27,28</sup> controlled the optimization. The phase map was displayed on the SLM using a graphics card (GeForce GT520, NVidia). A digital delay generator (DG645, Stanford Research Systems) controlled the synchronization between the laser and the oscilloscope. For linear PAWS, one pulse was fired every 20 ms. For nonlinear PAWS, two pulses were fired with a delay of 40  $\mu\text{s}$ , but the burst period remained at 20 ms. After optimization, the blood layer was moved off the optical path and a CCD camera attached to a microscope (resolution of 1  $\mu\text{m}/\text{pixel}$ ) was used to image the optical field at the ultrasound focal plane (Fig. 5), when the initial and final phase patterns were displayed on the SLM, respectively. By calculating the autocorrelation<sup>37</sup> of the initial speckle pattern, we measured the speckle grain size at the ultrasonic focal plane to be  $\sim 5$   $\mu\text{m}$ , which was consistent with the final experimental optical focus size. It should be noted that, in the present study, the initial speckle pattern was generated by displaying a scrambled (randomized) phase pattern on the SLM screen. We found that such a scrambled pattern resulted in a nearly identical optical intensity to that produced with a flat (uniform) pattern on the SLM, similar to that demonstrated in ref. 28. We think the

reason for this may be that the ground glass diffuser completely scrambled the optical wavefront and there were many speckle grains within the ultrasonic detection volume in our experiment.

**Transducer field calibration.** A 50 MHz focused ultrasonic transducer was used in the experiment. The transducer was modified in-house from a non-focusing transducer (V358, Panametrics NDT) by adding an acoustic focusing lens. Due to the high centre frequency, the typical method of characterizing the transducer using a hydrophone or a pulser-receiver cannot be used. Instead, we used acoustic phase conjugation from a metal ball (8 mm diameter)<sup>38,39</sup> to measure the acoustic focal zone. The transducer axial focus was measured to be 11.425 mm from the transducer and the lateral FWHM of the focal region was 65  $\mu\text{m}$ . See Supplementary Fig. 3 for more details.

Received 31 March 2014; accepted 4 December 2014;  
published online 19 January 2015

## References

- Bohren, C. F. & Huffman, D. R. *Absorption and Scattering of Light by Small Particles* (Wiley, 1998).
- Wang, L. V. & Wu, H.-I. *Biomedical Optics: Principles and Imaging* (John Wiley & Sons, 2007).
- Fenno, L., Yizhar, O. & Deisseroth, K. The development and application of optogenetics. *Ann. Rev. Neurosci.* **34**, 389–412 (2011).
- Galantha, E. I. *et al.* *In vivo* fiber-based multicolor photoacoustic detection and photothermal purging of metastasis in sentinel lymph nodes targeted by nanoparticles. *J. Biophoton.* **2**, 528–539 (2009).
- Vellekoop, I. M. & Mosk, A. P. Focusing coherent light through opaque strongly scattering media. *Opt. Lett.* **32**, 2309–2311 (2007).
- Xu, X., Liu, H. & Wang, L. V. Time-reversed ultrasonically encoded optical focusing into scattering media. *Nature Photon.* **5**, 154–157 (2011).
- Liu, H., Xu, X., Lai, P. & Wang, L. V. Time-reversed ultrasonically encoded (TRUE) optical focusing into tissue-mimicking media with optical thickness up to 70 mean free paths. *J. Biomed. Opt.* **16**, 086009 (2011).
- Lai, P., Xu, X., Liu, H., Suzuki, Y. & Wang, L. V. Reflection-mode time-reversed ultrasonically encoded (TRUE) optical focusing into turbid media. *J. Biomed. Opt.* **16**, 080505 (2011).
- Lai, P., Xu, X., Liu, H. & Wang, L. V. Time-reversed ultrasonically encoded (TRUE) optical focusing in biological tissue. *J. Biomed. Opt.* **17**, 030506 (2012).
- Suzuki, Y., Xu, X., Lai, P. & Wang, L. V. Energy enhancement in time-reversed ultrasonically encoded optical focusing using a photorefractive polymer. *J. Biomed. Opt.* **17**, 080507 (2012).
- Lai, P., Suzuki, Y., Xu, X. & Wang, L. V. Focused fluorescence excitation with time-reversed ultrasonically encoded light and imaging in thick scattering media. *Laser Phys. Lett.* **10**, 075604 (2013).
- Wang, Y. M., Judkewitz, B., DiMarzio, C. A. & Yang, C. Deep-tissue focal fluorescence imaging with digitally time-reversed ultrasound-encoded light. *Nature Commun.* **3**, 928 (2012).
- Si, K., Fiolka, R. & Cui, M. Fluorescence imaging beyond the ballistic regime by ultrasound-pulse-guided digital phase conjugation. *Nature Photon.* **6**, 657–661 (2012).

14. Judkewitz, B., Wang, Y. M., Horstmeyer, R., Mathy, A. & Yang, C. Speckle-scale focusing in the diffusive regime with time reversal of variance-encoded light (TROVE). *Nature Photon.* **7**, 300–305 (2013).
15. Hsieh, C.-L., Pu, Y., Grange, R. & Psaltis, D. Digital phase conjugation of second harmonic radiation emitted by nanoparticles in turbid media. *Opt. Express* **18**, 12283–12290 (2010).
16. Vellekoop, I. M., Cui, M. & Yang, C. Digital optical phase conjugation of fluorescence in turbid tissue. *Appl. Phys. Lett.* **101**, 081108 (2012).
17. Vellekoop, I. M. & Mosk, A. P. Phase control algorithms for focusing light through turbid media. *Opt. Commun.* **281**, 3071–3080 (2008).
18. Cui, M. Parallel wavefront optimization method for focusing light through random scattering media. *Opt. Lett.* **36**, 870–872 (2011).
19. Conkey, D. B., Brown, A. N., Caravaca-Aguirre, A. M. & Piestun, R. Genetic algorithm optimization for focusing through turbid media in noisy environments. *Opt. Express* **20**, 4840–4849 (2012).
20. Popoff, S. M. *et al.* Measuring the transmission matrix in optics: an approach to the study and control of light propagation in disordered media. *Phys. Rev. Lett.* **104**, 100601 (2010).
21. Kong, F. *et al.* Photoacoustic-guided convergence of light through optically diffusive media. *Opt. Lett.* **36**, 2053–2055 (2011).
22. Caravaca-Aguirre, A. M. *et al.* High contrast three-dimensional photoacoustic imaging through scattering media by localized optical fluence enhancement. *Opt. Express* **21**, 26671–26676 (2013).
23. Conkey, D. B. *et al.* Super-resolution photoacoustic imaging through a scattering wall. Preprint at <http://arXiv.org/abs/1310.5736> (2013).
24. Chaigne, T. *et al.* Improving photoacoustic-guided optical focusing in scattering media by spectrally filtered detection. *Opt. Lett.* **39**, 6054–6057 (2014).
25. Chaigne, T. *et al.* Controlling light in scattering media noninvasively using the photo-acoustic transmission-matrix. *Nature Photon.* **8**, 58–64 (2014).
26. Yao, J., Ke, H., Tai, S., Zhou, Y. & Wang, L. V. Absolute photoacoustic thermometry in deep tissue. *Opt. Lett.* **38**, 5228–5231 (2013).
27. Katz, O., Small, E., Broomberg, Y. & Silberberg, Y. Focusing and compression of ultrashort pulses through scattering media. *Nature Photon.* **5**, 372–377 (2011).
28. Tay, J. W., Lai, P., Suzuki, Y. & Wang, L. V. Ultrasonically encoded wavefront shaping for focusing into random media. *Sci. Rep.* **4**, 3918 (2014).
29. Hepler, L. G. Thermal expansion and structure in water and aqueous solutions. *Can. J. Chem.* **47**, 4613–4617 (1969).
30. Wang, S.-H., Wei, C.-W., Jee, S.-H. & Li, P.-C. Quantitative thermal imaging for plasmonic photothermal therapy. *J. Med. Biol. Eng.* **31**, 387–393 (2011).
31. Duck, F. A. *Physical Properties of Tissue* (Academic, 1990).
32. Mosk, A. P., Lagendijk, A., Lerosey, G. & Fink, M. Controlling waves in space and time for imaging and focusing in complex media. *Nature Photon.* **6**, 283–292 (2012).
33. Conkey, D. B., Caravaca-Aguirre, A. M. & Piestun, R. High-speed scattering medium characterization with application to focusing light through turbid media. *Opt. Express* **20**, 1733–1740 (2012).
34. *American National Standard for the Safe Use of Laser in Health Care Facilities, ANSI Z136.1.1* (American National Standards Institute, 2000).
35. Petrova, E. *et al.* Using optoacoustic imaging for measuring the temperature dependence of Grueneisen parameter in optically absorbing solutions. *Opt. Express* **21**, 25077–25090 (2013).
36. Tay, J. W., Taylor, M. A. & Bowen, W. P. Sagnac-interferometer-based characterization of spatial light modulators. *Appl. Opt.* **48**, 2236–2242 (2009).
37. Piederrière, Y. *et al.* Scattering through fluids: speckle size measurement and Monte Carlo simulations close to and into the multiple scattering. *Opt. Express* **12**, 176–188 (2004).
38. Kolosov, O. V., Lobkis, O. I., Maslov, K. I. & Zinin, P. V. The effect of the focal plane position on image of spherical object in the reflection acoustic microscope. *Acoust. Lett.* **16**, 84–88 (1992).
39. Maslov, K. I., Dorozhkin, L. M., Doroshenko, V. S. & Maev, R. G. A new focusing ultrasonic transducer and two foci acoustic lens for acoustic microscopy. *IEEE Trans. Ultrason. Ferroelectr. Freq. Control* **44**, 380–385 (1997).

### Acknowledgements

The authors thank K. Maslov for manufacturing the acoustic lens, C. Ma for assistance with acoustic focus calibration, T.-W. Wong for help with preparing the supplementary cartoons and J. Ballard for editing the manuscript. This work was sponsored in part by National Institutes of Health grants DP1 EB016986 (NIH Director's Pioneer Award) and R01 CA186567 (NIH Director's Transformative Research Award) as well as National Academies Keck Futures Initiative grant IS 13.

### Author contributions

P.L., J.W.T. and L.V.W. initiated the project. P.L. implemented the photoacoustically guided wavefront-shaping system. L.W. initiated the principle of dual-pulse photoacoustic nonlinearity based on the Grueneisen relaxation effect. J.W.T. wrote code for the experiment and simulations. P.L., J.W.T. and L.W. designed and ran the experiment, and prepared the manuscript. L.V.W. provided overall supervision. All authors were involved in analysis of the results and revision of the manuscript.

### Additional information

Supplementary information is available in the [online version](#) of the paper. Reprints and permissions information is available online at [www.nature.com/reprints](http://www.nature.com/reprints). Correspondence and requests for materials should be addressed to L.V.W.

### Competing financial interests

P.L., J.W.T. and L.V.W. declare no competing financial interests. L.V.W. has financial interests in Microphotoacoustics, Inc. and Endra, Inc., which, however, did not support this work.